

Quasinormal modes and absorption cross sections of Born-Infeld-de Sitter black holes

Nora Bretón ¹,

Dpto de Física, Centro de Investigación y de Estudios Avanzados del I.P.N., Apdo. 14-740, Mexico City, Mexico.

Tyler Clark ², & Sharmanthie Fernando ³

*Department of Physics, Geology & Engineering Technology
Northern Kentucky University
Highland Heights, Kentucky 41099, U.S.A.*

Abstract

In this paper, we have studied QNM modes and absorption cross sections of Born-Infeld-de Sitter black holes. WKB approximation is employed to compute the QNM modes of massless scalar fields. We have also used null geodesics to compute quasi-normal modes in the eikonal approximation. In the eikonal limit QNMs of black holes are determined by the parameters of the circular null geodesics. Unstable circular null orbits are derived from the effective metric which is obeyed by light rays under the influence of a nonlinear electromagnetic field. Comparison is shown with the QNM of the linear electromagnetic counterpart, the Reissner-Nordström black hole. Furthermore, the null geodesics are employed to compute the absorption cross sections in the high frequency limit via the sinc approximation.

Key words: Born-Infeld, absorption cross sections, scalar perturbations, WKB

1 Introduction

It is well known that the self-energy and the electric field diverges for a point charge in Maxwell's electrodynamics. In 1934, Born and Infeld developed a theory of nonlinear electrodynamics in order to obtain a finite value for the self-energy of a point charge [1]. The action for the Born-Infeld electrodynamics coupled to gravity with a cosmological constant is given by,

¹nora@fis.cinvestav.mx

²clarkt3@mymail.nku.edu

³fernando@nku.edu

$$S = \int d^4x \sqrt{-g} \left[\frac{R - 2\Lambda}{16\pi G} + L(F) \right] \quad (1)$$

where the function $L(F)$ is given by,

$$L(F) = 4b^2 \left(1 - \sqrt{1 + \frac{F}{2b^2} - \frac{G^2}{16b^4}} \right) \quad (2)$$

Here, $F = F^{\mu\nu} F_{\mu\nu}$ and $G = \tilde{F}^{\mu\nu} F_{\mu\nu}$. The dual tensor $\tilde{F}_{\mu\nu}$ is given by,

$$\tilde{F}_{\mu\nu} = \frac{\epsilon_{\mu\nu\rho\sigma} F^{\rho\sigma}}{2\sqrt{-g}} \quad (3)$$

b in the action is a parameter of the Born-Infeld non-linear electrodynamics and has the dimensions $length^{-2}$. When $b \rightarrow \infty$, the Lagrangian $L(F) \rightarrow -F$ which corresponds to Maxwell's electrodynamics. In flat space, the electric field strength E in Born-Infeld electrodynamics is given by, $E = Q/\sqrt{r^4 + \frac{Q^2}{b^2}}$ which is finite at $r = 0$. Among the appealing features of Born-Infeld electrodynamics include, the finiteness of energy density of charged particles, its relation to string theory, the electro magnetic duality [2], its exceptional properties of wave propagation and the absence of birefringes [3] [4].

In recent years, Born-Infeld theory has attracted considerable attention due to its role in string theory. For example, Leigh [5] showed that the low energy dynamics of D-branes could be described by a Dirac-Born-Infeld type action. The action for a massless vector field in open superstring theory is given by a modified Born-Infeld action as discussed by Tseytlin et.al. [6] [7]. Bergshoeff et.al. [8] showed that one-loop approximation to sigma-model perturbation theory of gauge fields in open-superstrings lead to the Born-Infeld action. A review of the Born-Infeld theory and string theory can be found in [9].

There are many interesting black hole solutions and physics related to Born-Infeld electrodynamics in the literature. Asymptotically flat charged black hole solutions in Born-Infeld gravity and the geodesics were presented by Bretón in [10]. Test particle motion around Born-Infeld black holes were studied by Linares et.al. [11]. Null geodesics of Born-Infeld black holes were studied by Fernando [12].

Stability and quasi-normal modes of the asymptotically flat charged black hole in Born-Infeld gravity were studied by Fernando et.al. in [13][14][15]. Nariai black holes of Born-Infeld black holes in de Sitter space were studied by Fernando [16]. Energy decomposition in Born-Infeld charged black holes were presented in [17] and the energy extraction from the Born-Infeld black holes was studied in [18]

Melvin universe in Born-Infeld electrodynamics was studied by Gibbons and Herderio [19]. Charged black hole solutions in Lovelock-Born-Infeld black holes in 5 dimensions were studied by Aiello et.al [20]. Attractor mechanism for extreme black hole

solutions in Einstein-Born-Infeld-dilaton gravity was studied in [21]. There are several works to present black hole solutions in Born-Infeld theory coupled to Einstein gravity with a cosmological constant [22][23][24][25].

Studying quasi normal modes (QNM) of a black hole is an well established subject. When a black hole is perturbed by fields of various spins or by perturbing the metric, there are oscillations with complex frequencies. Such frequencies depend only on the black hole and the corresponding field parameters. When two black holes merge, as the historic event that occurred in 2015 creating gravitational waves, the intermediate signals correspond to the QNM's [26]. Hence, it would be important to calculate QNM frequencies in alternative theories such as general relativity coupled to Born-Infeld theory to see if there are deviations from the usual general relativity coupled to Maxwell's theory. Hence there is strong motivation to study and calculate QNM's of black holes in theories such as Born-Infeld-de Sitter black holes. There are many works in the literature to compute QNM frequencies of variety of perturbations. For example, QNM frequencies of canonical acoustic holes (black hole analogue) were calculated by Dolan et.al.[27]. QNM's of regular black hole with a magnetic charge were calculated by Li et.al.[28]. A comparison of different cosmological models were done using QNM's of the Schwarzschild-de Sitter black hole by Chirenti et.al.[29]. QNM's of Schwarzschild black holes were calculated by a matrix method by Lin and Qian[30]. A "generalized continued fraction method " was employed to compute QNM frequencies of an extreme Reissner-Nordstrom and Kerr black hole by Richartz [31]. A new approach, "Asymptotic Iteration Method" was used to calculate black hole QNM's by Cho et.al.[32]. There are several works on QNM's of de Sitter black holes by Konoplya [33][34][35][36]. There are so many works on this topic that there is not sufficient space to mention all of them here; there is an excellent review on QNM's of black holes and black branes by Berti et.al.[37].

In this paper we are interested in computing QNM's and absorption cross sections of Born-Infeld black hole with a cosmological constant. As is well known, the current universe is expanding at an accelerated rate [38][39][40][41][42]. The simplest explanation for the acceleration is the existence of a cosmological constant. Hence it becomes timely to study black holes with a cosmological constant.

The paper is organized as follows: In section 2, an introduction to the Born-Infeld-de Sitter black hole is given. In section 3 the massless scalar field perturbation is introduced. In section 4, the QNM frequencies are calculated via the WKB approximation for various parameters of the theory. In section 5, the QNM's are calculated via the null geodesics of the Born-Infeld-de Sitter black hole. In section 6, the absorption cross section via the null geodesics are computed and presented. Finally, the conclusion is given in section 7.

2 Introduction to Born-Infeld-de Sitter black holes

In this section, we will present the Born-Infeld-de Sitter black hole solutions and some important properties. The metric of the static charged, spherical symmetric black hole derived from the action in eq.(1) for $F \neq 0$ and $G = 0$ is given by,

$$ds^2 = -f(r)dt^2 + f(r)^{-1}dr^2 + r^2(d\theta^2 + \sin^2\theta d\varphi^2) \quad (4)$$

with,

$$f(r) = 1 - \frac{2M}{r} - \frac{\Lambda r^2}{3} + \frac{2b^2}{3} \left[r^2 - \sqrt{r^4 + Q^2/b^2} \right] + \frac{2Q^2}{3r} \sqrt{\frac{b}{Q}} F \left[\arccos \left(\frac{r^2 - Q/b}{r^2 + Q/b} \right), \frac{1}{\sqrt{2}} \right], \quad (5)$$

We have used the elliptic function F in the above equation. In the literature, the function $f(r)$ is also written in terms of the Hypergeometric function ${}_2F_1$. For the sake of completeness we want to point out that the relationship between the elliptic function and the hypergeometric function is given as follows:

$$\int_r^\infty \frac{ds}{\sqrt{Q^2/b^2 + s^4}} = \frac{1}{r} {}_2F_1 \left[\frac{1}{4}, \frac{1}{2}; \frac{5}{4}; -\frac{Q^2}{b^2 r^4} \right] = \frac{1}{2} \sqrt{\frac{b}{Q}} F \left[\arccos \left(\frac{r^2 - Q/b}{r^2 + Q/b} \right), \frac{1}{\sqrt{2}} \right], \quad (6)$$

The parameters in the metric are as follows; M is the mass, Q is the electric charge, b is the non-linear parameter and Λ is the cosmological constant. The electric field strength for the black hole space-time is given by,

$$E = \frac{Q}{\sqrt{r^4 + \frac{Q^2}{b^2}}} \quad (7)$$

In the limit $b \rightarrow \infty$, the metric function $f(r)$ can be expanded to give,

$$f(r)_{RN} = 1 - \frac{2M}{r} + \frac{Q^2}{r^2} - \frac{\Lambda r^2}{3} \quad (8)$$

which is the function $f(r)$ for the Reissner-Nordstrom-de Sitter black hole for Maxwell's electrodynamics. When $r \rightarrow 0$, the function $f(r)$ has the behavior,

$$f(r) \approx 1 - \frac{(2M - \alpha)}{r} - 2bQ + \frac{r^2}{3}(2b^2 - \Lambda) + \mathcal{O}(r^3) \quad (9)$$

Where,

$$\alpha = \frac{1}{3} \sqrt{\frac{b}{\pi}} Q^{3/2} \Gamma \left(\frac{1}{4} \right)^2 \quad (10)$$

The singular nature of the black holes depends on the relative values of the parameters M and α , as described below:

Case 1: ($M > \frac{\alpha}{2}$)

In this case, for $r \rightarrow 0$, $f(r) \rightarrow -\infty$; the black hole will behave similar to the Schwarzschild-de Sitter black hole as given in the Fig(1). It is possible to have two horizons, an event horizon (r_h) and a cosmological horizon(r_c). It is also possible to have extreme black holes with one degenerate horizon. For large masses, there won't be any horizons and there will be naked singularities.

Case 2: ($M < \frac{\alpha}{2}$)

Here, for $r \rightarrow 0$, $f(r) \rightarrow \infty$; the behavior of the black hole will be similar to the Reissner-Nordstrom-de Sitter black hole (RNdS black hole) as shown in Fig(2). As one can observe, there are many possibilities for this geometry. First, it is possible to have three horizons with the largest one being the cosmological constant. It is possible to have extreme black holes where there are only two horizons exists. For special parameters, a degenerate horizon exists with one horizon. All these possibilities are given in Fig.(2).

Case 3: ($M = \frac{\alpha}{2}$)

Here, for $r \rightarrow 0$, $f(r) \rightarrow (1 - 2Q\beta)$; $f(r)$ is finite at $r = 0$ and single valued as given in Fig.(3). The Kretschmann scalar diverge at $r = 0$ for these black holes; so, the singularity exists.

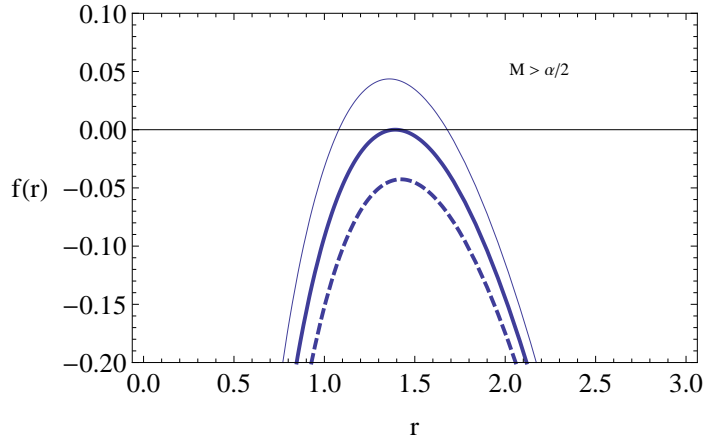


Figure 1: The figure shows $f(r)$ vs r when $M > \frac{\alpha}{2}$. Here, $\Lambda = 0.5, b = 1.4$ and $Q = 0.2308$

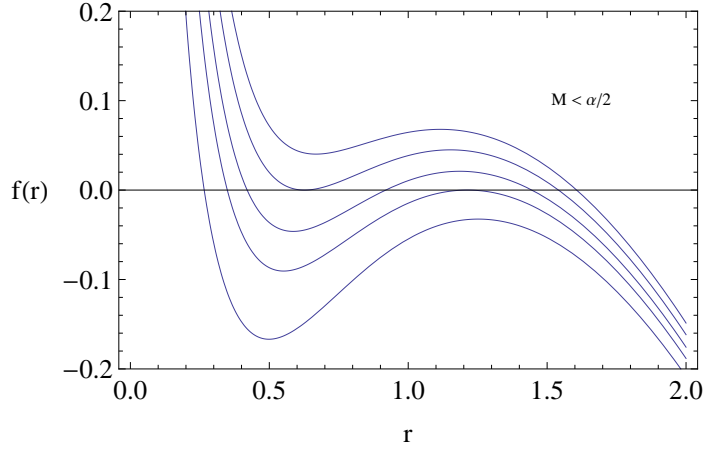


Figure 2: The figure shows $f(r)$ vs r when $M < \frac{\alpha}{2}$. Here, $\Lambda = 0.5, b = 1.4$ and $Q = 0.63079$

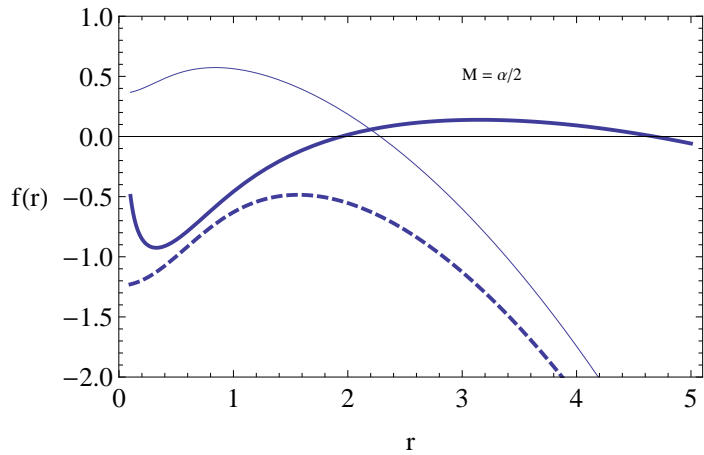


Figure 3: The figure shows $f(r)$ vs r when $M = \frac{\alpha}{2}$. Here, $b = 1.5$

In comparison with the Reissner-Nordstrom-de Sitter black hole, the geometry seems to be different mostly closer to the horizons as shown in Fig(4).

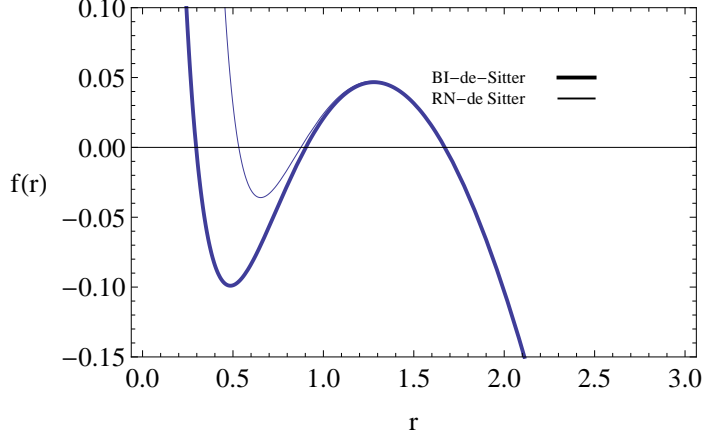


Figure 4: The figure shows $f(r)$ vs r for BIdS and RNdS black holes. Here $M = 0.593$, $Q = 0.6$, $\Lambda = 0.45$ and $b = 1.4$

3 Massless scalar field perturbations

In this section, we will focus on perturbations by a minimally coupled massless scalar field in the fixed background of the Born-Infeld-de Sitter black hole (BIdS black hole). The equations of motion of the minimally coupled scalar field is given by the Klein-Gordon equation, $\nabla^2\Phi = 0$. The scalar field Φ can be decomposed to its partial modes in terms of spherical harmonics, $Y_{l,m}(\theta, \phi)$ as,

$$\Phi(r, \theta, \phi, t) = \sum_{l,m} e^{-i\omega t} Y_{l,m}(\theta, \phi) \frac{R(r)}{r} \quad (11)$$

Here, l and m are the angular and the magnetic quantum numbers respectively. ω is the oscillating frequency of the scalar field. With the decomposition in eq(11), the Klein-Gordon equation will separate into radial equation given by,

$$\frac{d^2 R(r_*)}{dr_*^2} + (\omega^2 - V_{scalar}(r_*)) R(r_*) = 0 \quad (12)$$

Here r_* is the tortoise coordinates which is given by, $dr_* = \frac{dr}{f(r)}$ and V_{scalar} is given by,

$$V_{scalar}(r) = f(r) \left(\frac{l(l+1)}{r^2} + \frac{f'(r)}{r} \right) \quad (13)$$

The function $f(r)$ is zero at the event horizon, r_h and at the cosmological horizon r_c . Therefore, $V_{scalar}(r_h) = V_{scalar}(r_c) = 0$. It is not possible to calculate $R(r_*)$ analytically; we can get an approximation by expanding $f(r)$ around $r = r_h$ and $r = r_c$ in a Taylor series as,

$$f(r) \approx f'(r_h)(r - r_h) \quad (14)$$

$$f(r) \approx f'(r_c)(r - r_c) \quad (15)$$

Since $f'(r_c) < 0$, r_* closer to $r = r_c$ can be written as,

$$r_* \approx -\frac{1}{|f'(r_c)|} \text{Log}(r_c - r) \quad (16)$$

Hence, for $r \rightarrow r_c$, $r_* \rightarrow \infty$. Since $f'(r_h) > 0$, r_* closer to $r = r_h$ can be written as,

$$r_* \approx \frac{1}{|f'(r_h)|} \text{Log}(r - r_h) \quad (17)$$

Hence, for $r \rightarrow r_h$, $r_* \rightarrow -\infty$. Hence the effective potential $V_{scalar} \rightarrow 0$ when $r_* \rightarrow \pm\infty$.

4 QNM frequencies of the scalar field by the WKB approximations

QNM frequencies of the scalar perturbations can be computed by imposing proper boundary conditions on the solutions of the eq(12). Usually, eq(12) cannot be solved analytically. There are few exactly solvable perturbation equations in the literature. In 2 +1 dimensions, exact QNM values have been found for black holes with a dilaton field by Fernando [43][44][45].

The boundary conditions imposed for an asymptotically de Sitter black hole space-time goes like this: the field has to be purely ingoing at the black hole event horizon, r_h and the field has to be purely outgoing at the cosmological horizon, r_c . With such boundary conditions, $R(r_*)$ behaves as,

$$R(r_*) \rightarrow \exp(i\omega r_*); \quad r_* \rightarrow -\infty (r \rightarrow r_h) \quad (18)$$

$$R(r_*) \rightarrow \exp(-i\omega r_*); \quad r_* \rightarrow +\infty (r \rightarrow r_c) \quad (19)$$

When such boundary conditions are imposed, the resulting frequencies, ω are complex. As it is clear from section(4.1), the effective potential V_{scalar} has a peak and acts as a barrier to the scalar field in the background of the black hole geometry. In this scenario one can employ the WKB approximation to compute ω . Iyer and Will developed it for third order in [46] and was extended to sixth order by Konoplya in [47]. WKB approximation has been employed to study QNM in many papers including [48] [49] [50] .

In the sixth order WKB approach, QNM frequencies are given by the expression,

$$\omega^2 = -i\sqrt{-2V''(r_m)} \left(\sum_{i=2}^6 \mathcal{T}_i + n + \frac{1}{2} \right) + V(r_m) \quad (20)$$

Here $V(r)$ is the effective potential for the corresponding equations, r_m is where $V(r)$ reach a maximum and $V''(r)$ is the second derivative of the potential. Expressions for \mathcal{T}_i can be found in [47].

4.1 Effective potentials

In this section we will focus on the properties of the effective potential of the scalar field. V_{scalar} is plotted for the parameters in the theory, M, Q, l, b and Λ . In Fig(5), the potential is plotted for various values of the charge Q . When Q increases, the height of the potential increases. In Fig(6), the potential is plotted for various values of l . For $l > 0$, the potential is positive in the region between the horizons and the height of the potential increases with l . On the left hand side, the potential is plotted for $l = 0$. It has a local minimum between the horizons and is negative in one part of the region. Such behavior for $l = 0$ scalar field potential is common for black holes with a positive cosmological constant [48]. In Fig(7), the potential is plotted by varying the mass. When the mass is higher, the height of the potential is lower. In Fig(8), the potential is plotted by varying the non-linear parameter b . When b increases, the height increases. Hence one can conclude that the height of the potential of the Reissner-Nordstrom-de Sitter black hole is higher than the Born-Infeld-de Sitter black hole with the same charge. In Fig(9), the potential is plotted to understand how it behaves with Λ . For higher Λ , the potential has a lower height.

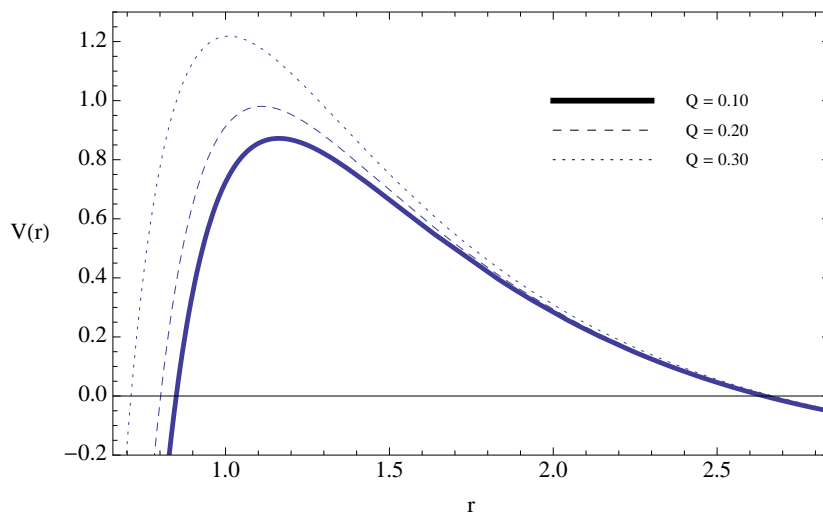


Figure 5: The figure shows $V(r)$ vs r for massless scalar field for varying charge Q . Here, $\Lambda = 0.3, b = 1, M = 0.4, l = 2$

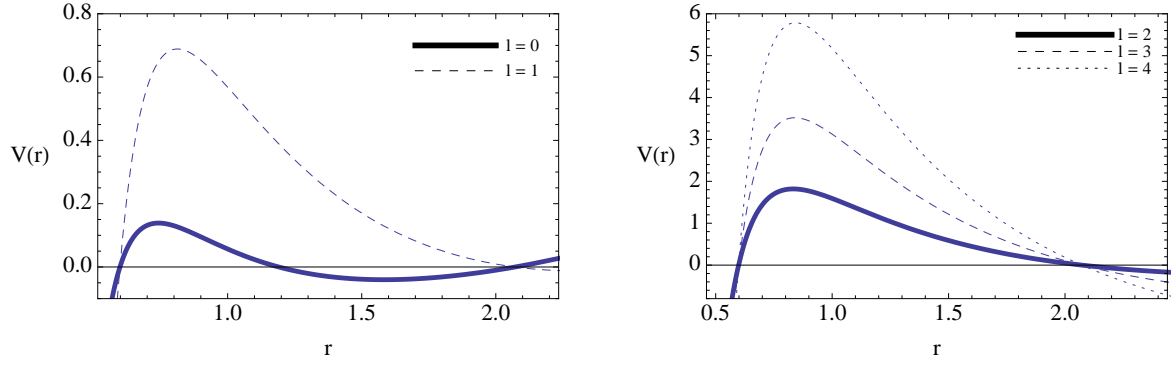


Figure 6: The figure shows $V(r)$ vs r for massless scalar field for varying l . Here, $\Lambda = 0.5, b = 1, M = 0.3, Q = 0.15$

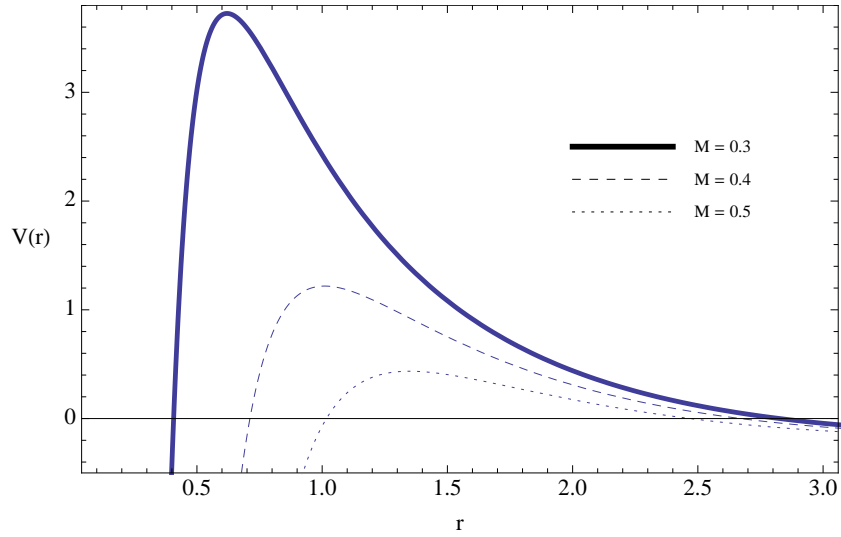


Figure 7: The figure shows $V(r)$ vs r for massless scalar field for varying M . Here, $\Lambda = 0.3, b = 1, Q = 0.3, l = 2$

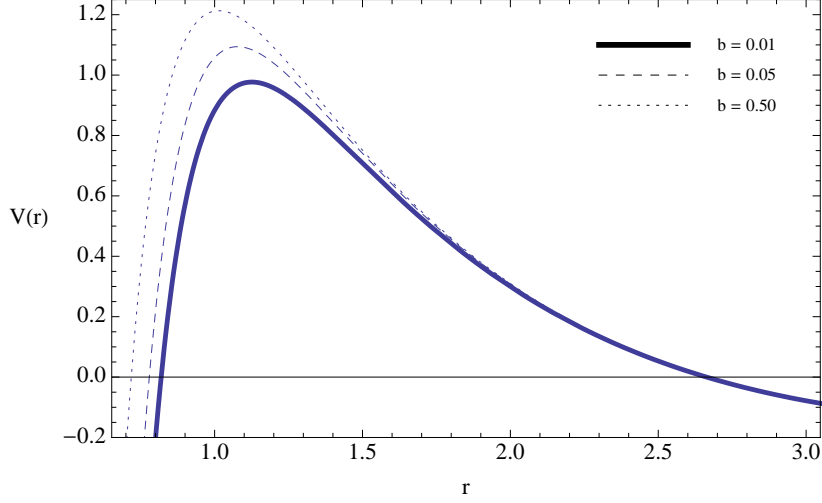


Figure 8: The figure shows $V(r)$ vs r for massless scalar field for varying b . Here, $\Lambda = 0.3, Q = 0.3, M = 0.4, l = 2$

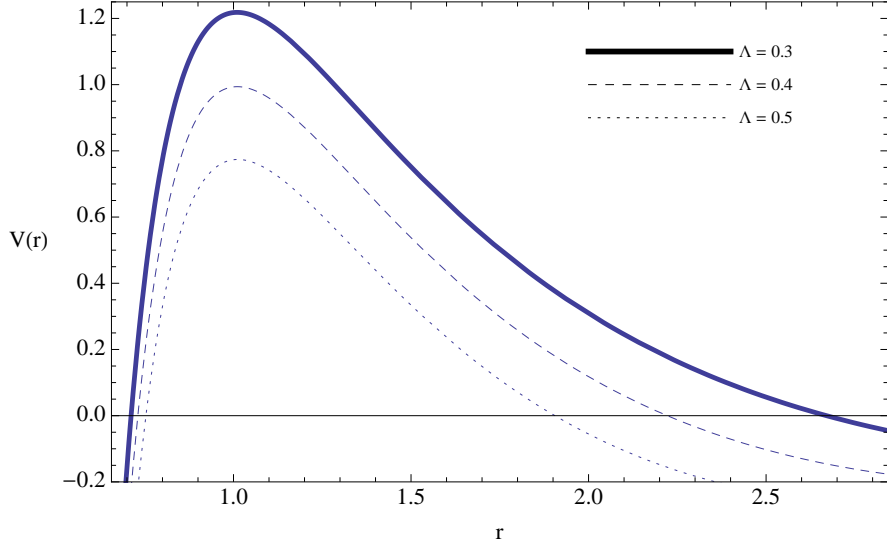


Figure 9: The figure shows $V(r)$ vs r for massless scalar field for varying Λ . Here, $Q = 0.3, M = 0.4, l = 2, b = 1$

4.2 QNM frequencies for each parameter in the theory

In this section, we will discuss the QNM frequencies for each parameter in the theory. It is noted that all calculated values, ω_i is negative. Hence the black hole is stable for the massless scalar field for $l > 0$. Due to the nature of the potential for $l = 0$

case, the WKB approximation cannot be used to calculate the QNM values for that particular case. Hence all our calculations are for $l > 0$ and the one for $l = 0$ case is left for future studies. Also, unless mentioned the ω is calculated for the fundamental harmonic $n = 0$ case.

In Fig(10), ω is presented for varying Q . Both ω_r and ω_i increases with Q . Hence the field decay faster for large charge.

Quality Factor: One can define a quantity called the ‘‘Quality Factor’’ or the Q factor for any resonating system. For a standard harmonic oscillator Q factor determines the qualitative behavior of the oscillator. A system with low Q factor is said to be over damped and a system with high Q factor is said to be under damped. Along those lines, it is interesting to compare oscillatory nature of the scalar field in the black hole background in this work for various parameters. Here the Q factor is defined as [51]

$$Quality\ Factor = \frac{\omega_r}{2|\omega_i|} \quad (21)$$

If the Quality Factor is large, then the scalar field is a better oscillator in the given black hole background.

In Fig(11), the Quality Factor is plotted for varying charge Q . It increases when Q increases. Hence, the scalar field is a better oscillator for large charge.

Next we computed ω by changing the cosmological constant Λ as is given in Fig(12). Both ω_r and ω_i decreases as Λ increases; a black hole with smaller Λ is more stable for scalar perturbations. When the Quality Factor is observed, one could see that it decreases with Λ ; the scalar field is a better oscillator for small Λ .

We studied the behavior of ω with respect to b in Fig(14) and Fig(15). The real part of ω increases and reach a stable value for large b . The imaginary part of ω increases to reach a maximum and then decreases to reach a stable value. Since for $b \rightarrow \infty$, the BIdS black hole behaves like the RNdS black hole, the stable value is expected to be the one for the RNdS value for the same parameters given by, $\omega_{RNdS} = 0.95471 - i0.16272$. The BIdS black hole is most stable for the maximum value of ω_i . Also, BIdS black hole oscillates with less frequency compared to the RNdS black hole. The Quality Factor increases with b . Hence the scalar field is a better oscillator in the RNdS black hole back ground compared to its behavior in the BIdS black hole back ground.

Next we analyzed ω with respect to l ; ω_r and ω_i are plotted in Fig(16) for both $n = 0$ and $n = 1$. ω_r increases linearly with l where as ω_i decreases with l to reach stable value. The black hole is stable for small l .

In Fig(17), ω vs n is plotted to establish how the black hole oscillates for higher harmonics. Since the accuracy of the WKB approximation is higher for $l > n$, we have chosen $l =$ for this calculation. Here ω_r decreases with n ; the scalar field oscillates more for lower harmonics which is opposite for standing waves for a string. ω_i increases with n , and, hence the field decays faster for higher harmonics.

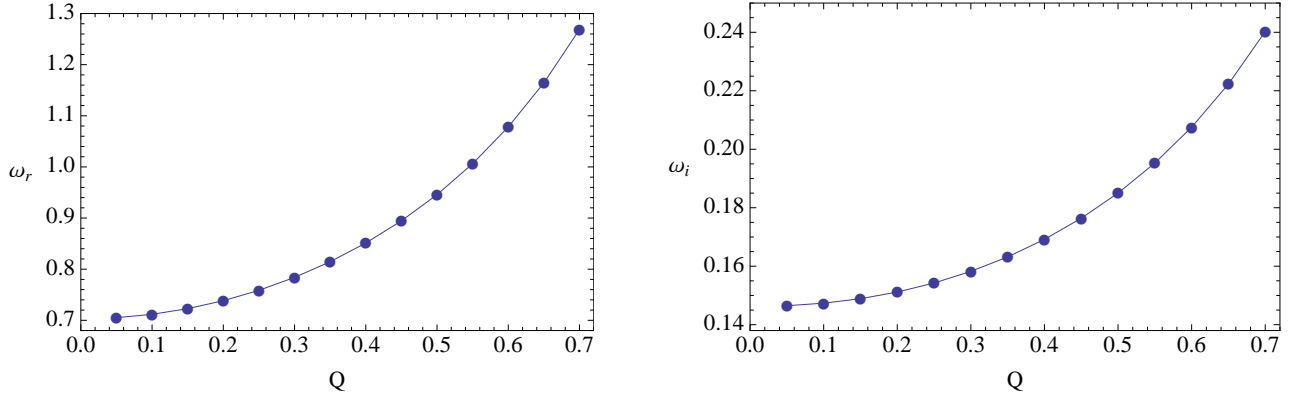


Figure 10: The figure shows ω vs Q for massless scalar field. Here $M = 0.5, l = 2, \Lambda = 0.2, \beta = 0.1$

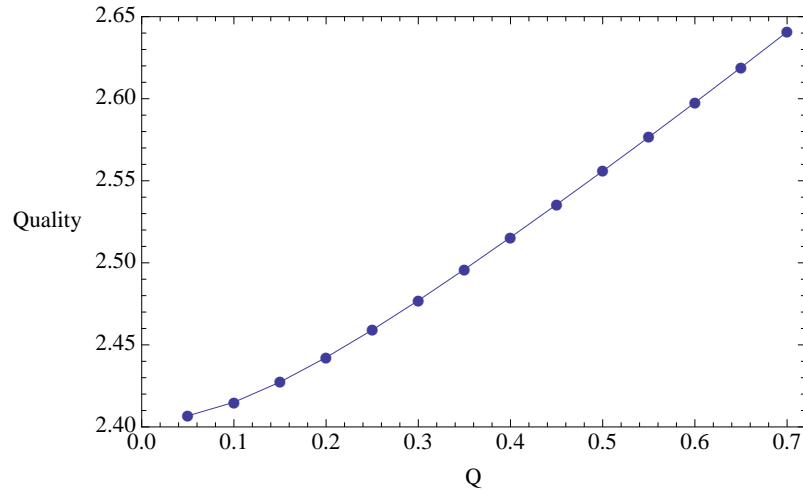


Figure 11: The figure shows Quality Factor vs Q for massless scalar field

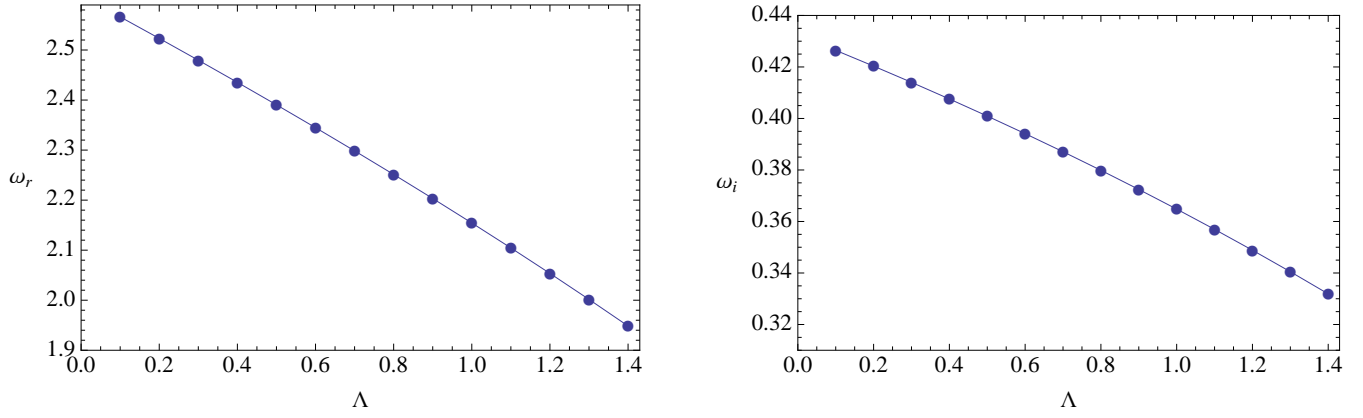


Figure 12: The figure shows ω vs Λ for massless scalar field. Here $M = 0.5, l = 2, Q = 0.45, \beta = 0.2$

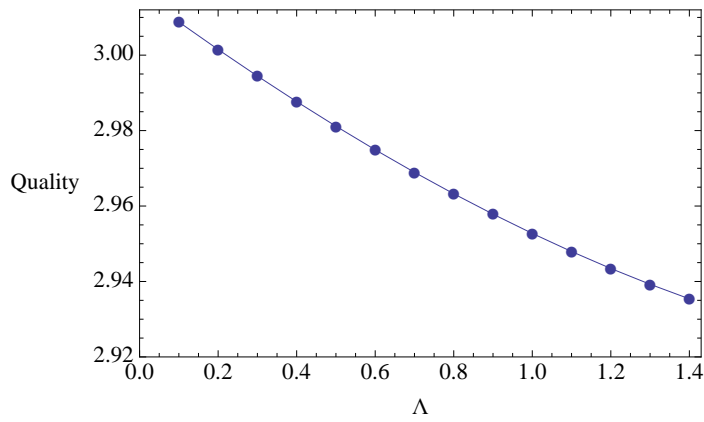


Figure 13: The figure shows Quality Factor vs Λ for massless scalar field

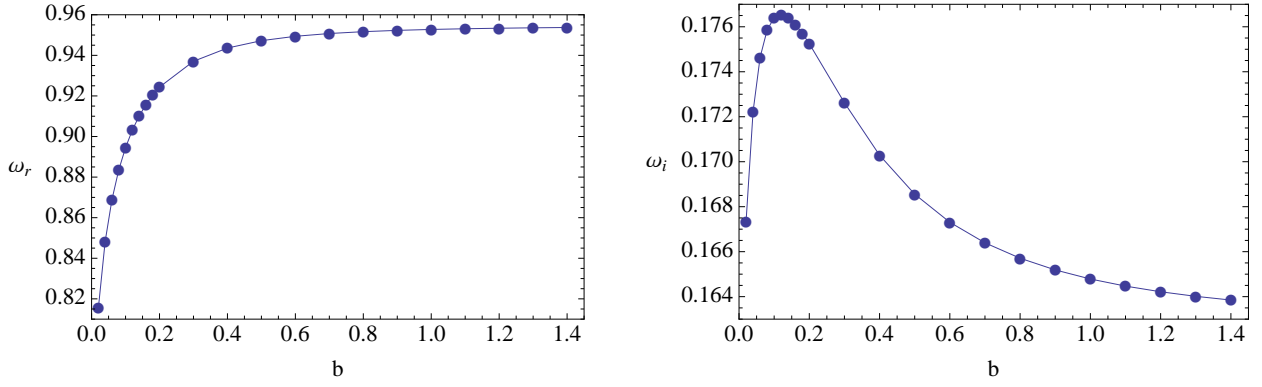


Figure 14: The figure shows ω vs b for massless scalar field. Here $M = 0.5, l = 2, \Lambda = 0.2, Q = 0.45$

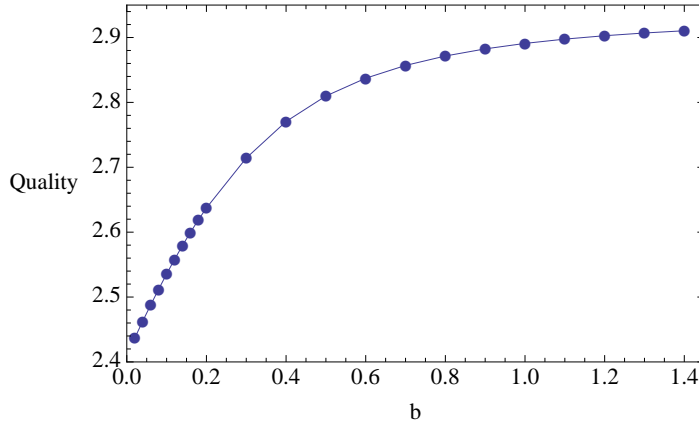


Figure 15: The figure shows Quality Factor vs b for massless scalar field

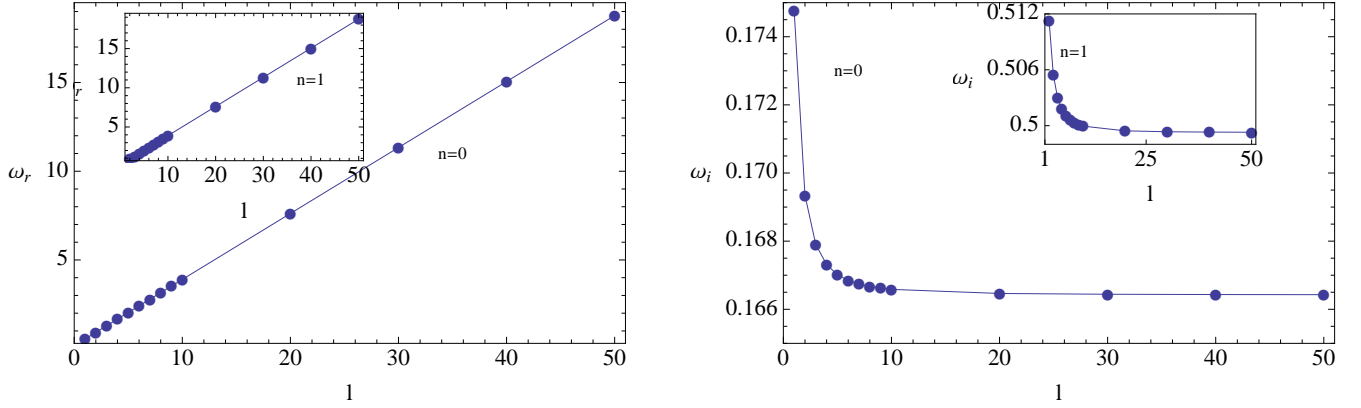


Figure 16: The figure shows ω vs l for massless scalar field. Here $M = 0.7, Q = 1, \Lambda = 0.2, \beta = 0.1$

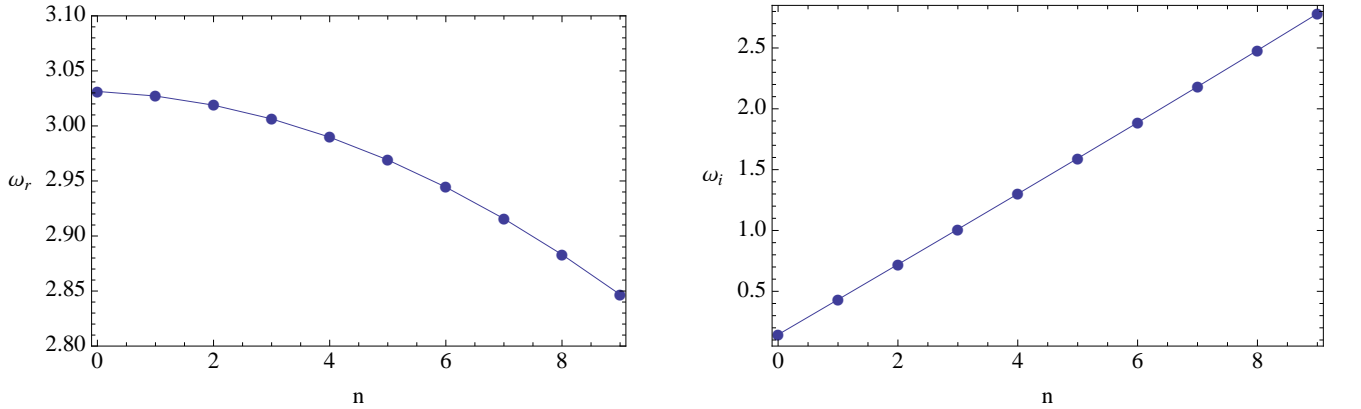


Figure 17: The figure shows ω vs n for massless scalar field. Here $M = 0.5, l = 10, \Lambda = 0.2, \beta = 0.2, Q = 0.1$

5 QNMs from massless test particles and photons in the eikonal approximation

Motion of massless test particles and photons in the black hole geometry are described by the null geodesics. In the eikonal limit, i.e. when $l \gg 1$, the QNM frequencies of a black hole can be determined by the parameters of null geodesics [52] [53]. More specifically, the angular velocity at the unstable null geodesic, Ω_a and the Lyapunov exponent, λ_{Ly} are related to the QNM frequencies as follows:

$$\omega_{QNM} = \Omega_a l - i(n + \frac{1}{2})|\lambda_{Ly}|, \quad (22)$$

Here λ_{Ly} in a dynamical system is a quantity that measure the average rate at which the nearby trajectories converge or diverge in the phase space. If a system has a positive Lyapunov exponent, it means that the nearby trajectories are diverging. Quantitative expressions for Ω_a and λ_{Ly} will be defined at a later stage in this section. There are several papers which have employed this method for computing QNM frequencies [54] [55] [56] [57].

In the BIdS black hole space-time, for some sets of values of the parameters, the effective potential experienced by a massless test particle may present a maxima and therefore the possibility for the existence of unstable geodesics. The equation for the null geodesics in the black hole background is given by,

$$\dot{r}^2 + V_{\text{null}} = E^2, \quad (23)$$

where,

$$V_{\text{null}} = \left(\frac{L^2}{r^2}\right) f(r), \quad (24)$$

with L denoting the angular momentum of the test particle and $f(r)$ is the metric function in eq. (4). The radius at which the effective potential is maximum is found using the condition that the first derivative of V is zero; this leads to the equation,

$$2f(r) - rf'(r) = 0. \quad (25)$$

The solution to eq(25) is denoted as r_{null} . Eq(25) for the BIdS metric is simplified to be,

$$r - 3M + Q^2 \sqrt{\frac{b}{Q}} F \left[\arccos \left(\frac{r^2 - Q/b}{r^2 + Q/b} \right), \frac{1}{\sqrt{2}} \right] = 0. \quad (26)$$

In the presence of nonlinear electromagnetic field, the behavior of photons and massless test particles are not the same. Photons do not follow the null geodesics of the black hole metric. Instead, they follow the null geodesics of an effective metric [58] [59], and unstable null geodesics of the corresponding modified effective potential are not the same as the ones for the BIdS metric with eqs. (4) and (5). The effective metric in nonlinear electrodynamics, which determines the light ray trajectories, is given by

$$ds_{\text{eff}}^2 = \frac{G_m}{G_e} [-f(r)dt^2 + f(r)^{-1}dr^2] + r^2 d\Omega^2, \quad (27)$$

where the factors G_e, G_m , correspond to the electric and magnetic charge modification introduced by the nonlinear field; they are given by

$$G_e = 1 - 4L_{FF} \frac{Q_m^2}{L_F^3 r^4}, \quad G_m = 1 + 4L_{FF} \frac{Q_m^2}{L_F r^4}, \quad (28)$$

where $L(F)$ is the nonlinear electromagnetic Lagrangian and L_F, L_{FF} are its first and second derivatives with respect to F ; here F is the the electromagnetic invariant, $F = 2(B^2 - E^2)$. For the BIIdS metric, with only electric charge, those factors are

$$G_m = 1, \quad G_e = 1 + \frac{Q^2}{b^2 r^4}. \quad (29)$$

Accordingly, the effective potential for light rays (photons) in the nonlinear electromagnetic space-time is given by

$$V_{\text{photons}} = \frac{G_e}{G_m} \left(\frac{L^2}{r^2} \right) f(r). \quad (30)$$

Hence the equation for the radius corresponding to the maximum value of the potential, r_{null} will be modified as

$$\left(\frac{G_e}{G_m} \right) \left(\frac{f'}{f} - \frac{2}{r} \right) - \left(\frac{G_e}{G_m} \right)' = 0, \quad (31)$$

which will lead to,

$$\begin{aligned} & 3(r^5 - 3Mr^4 - \frac{Q^2}{b^2}r + M\frac{Q^2}{b^2}) + 2\Lambda\frac{Q^2}{b^2}r^3 - 4Q^2r[r^2 - \sqrt{r^4 + Q^2/b^2}] \\ & + Q^2(3r^4 - \frac{Q^2}{b^2})\sqrt{\frac{b}{Q}}F \left[\arccos \left(\frac{r^2 - Q/b}{r^2 + Q/b} \right), \frac{1}{\sqrt{2}} \right] = 0. \end{aligned} \quad (32)$$

In Fig.(18) r_{null} as a function of the charge Q for massless particles is displayed. The maxima of the effective potentials for the RNdS and BIIdS are compared as a function of Q . As Q grows r_{null} decreases. The decreasing of r_{null} indicates that the photosphere is closer to the horizon r_h . Then for the same charge the photosphere is closer to the RNdS horizon than to the BIIdS one. In Fig.(19) r_{null} as a function of the charge Q is shown for BIIdS. Comparison is done between r_{null} for massless test particles and photons, as a function of Q for different values of Λ . The two upper curves are for photons while the lower one is for massless test particles. Photons are in fact affected when Λ varies, while the maxima of the effective potential does not change with Λ for massless test particles. This effect can be noticed by comparing eq.(32) for photons with the eq.(26) for massless particles, since Λ does not appear in the latter. As Q grows r_{null} decreases. In Fig.(20) the behavior of r_{null} for photons as a function of Λ is shown. This is the plot of the root of eq.(32). In this case negative values of Λ are also included for the sake of completeness. The values of the rest of parameters are fixed as $M = 0.6, Q = 0.6, b = 1.4$, and $-0.5 < \Lambda < 0.5$.

In the eikonal approximation the Lyapunov exponent for massless test particles is given by

$$\lambda_{\text{Ly}} = \sqrt{\frac{-V''_{\text{null}}(r_{\text{null}})r_{\text{null}}^2 f(r_{\text{null}})}{2L^2}}. \quad (33)$$

When V''_{null} for the BI_dS metric is substituted, the Lyapunov exponent is given by

$$\lambda_{\text{Ly}}^2 = \frac{f(r)}{r^2} \left(3 - \frac{12M}{r} + \frac{2Q^2}{\sqrt{r^4 + Q^2/b^2}} + \frac{4Q^2}{r} \sqrt{\frac{b}{Q}} F \left[\arccos \left(\frac{r^2 - Q/b}{r^2 + Q/b} \right), \frac{1}{\sqrt{2}} \right] \right) \quad (34)$$

The above expression evaluated at r_{null} . In Figs.(21),(22), (23) and (24) the Lyapunov exponent is displayed for various values of parameters. In Fig.(21) the Lyapunov exponents of BI_dS and RN_dS are compared for massless particles. For $Q = 0$ both curves start at the same point, that is the Lyapunov exponent of the Schwarzschild-de Sitter black hole for the same mass. For this case, the values of the parameters are, $M = 0.25, \Lambda = 0.1, b = 1$. The allowed range of Q is shorter for RN_dS than for BI_dS: $0 < Q < 0.3$. Fig.(22) is similar to Fig.(21) but for a different value of the mass, $M = 0.6$. As the mass grows, the behavior of the Lyapunov exponent of BI_dS approaches the one of RN_dS.

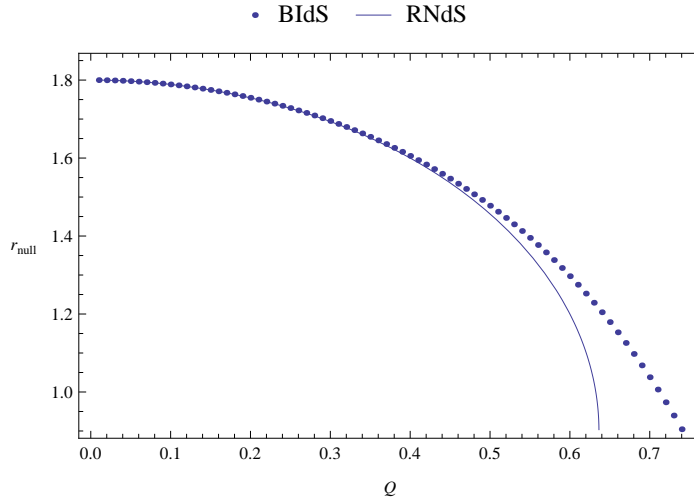


Figure 18: The figure shows r_{null} vs Q for massless particles. Here, $\Lambda = 0.1, b = 0.3$ and $M = 0.6$

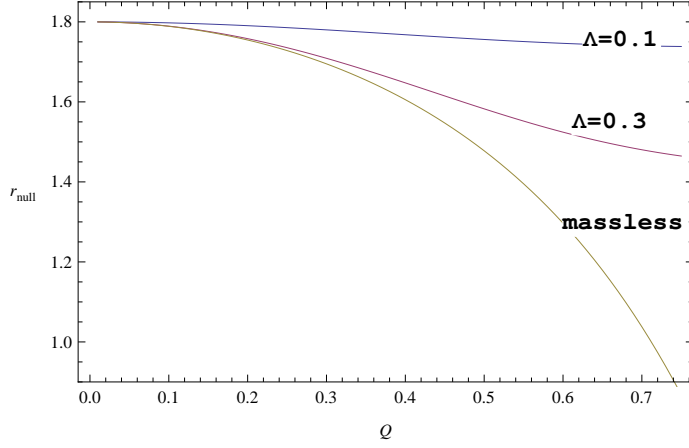


Figure 19: The figure shows r_{null} vs Q . The lower one is for massless particles and the upper two are for photons. Here, $M = 0.6, b = 0.3$

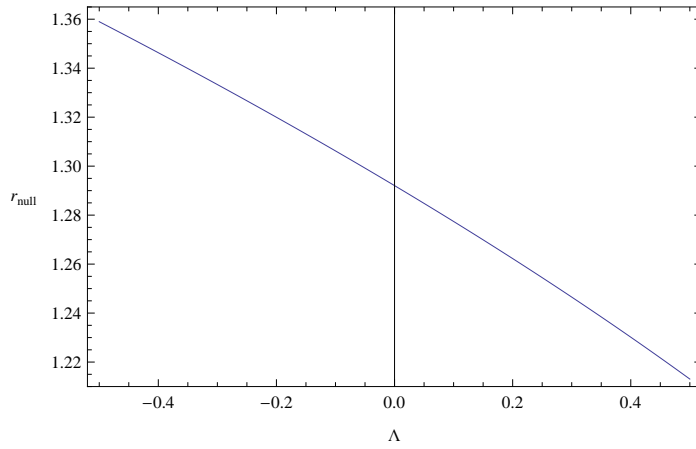


Figure 20: The figure shows r_{null} vs Λ . Here, $M = 0.6, Q = 0.6, b = 1.4$ and $-0.5 < \Lambda < 0.5$.

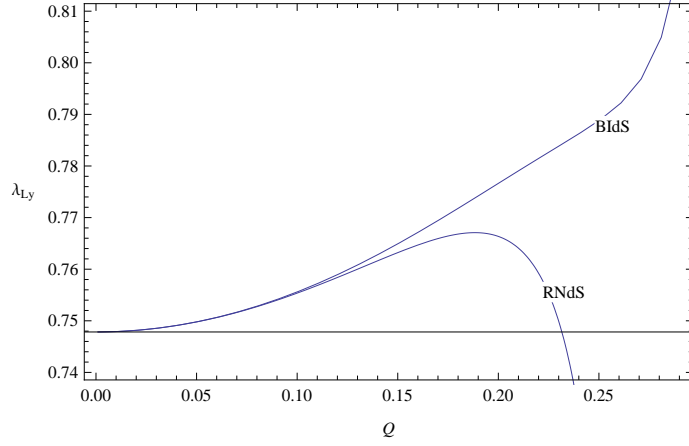


Figure 21: The figure shows λ_{Ly} vs Q for massless particles for BIdS and RNdS black holes. Here $M = 0.25$, $\Lambda = 0.1$, $b = 1$

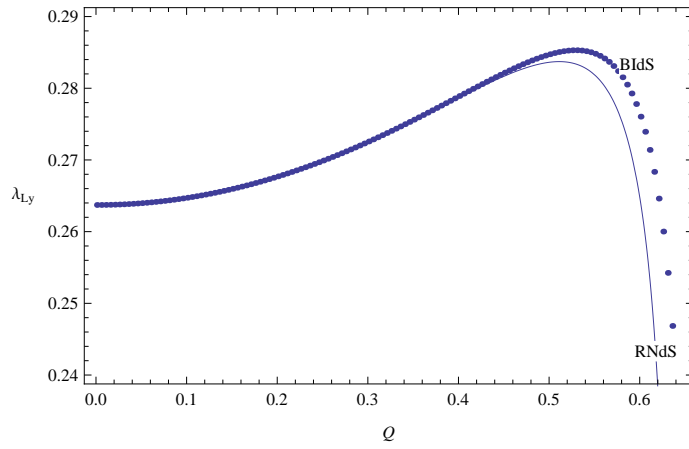


Figure 22: The figure shows λ_{Ly} vs Q for massless particles for BIdS and RNdS black holes. Here $M = 0.6$, $\Lambda = 0.1$, $b = 1$

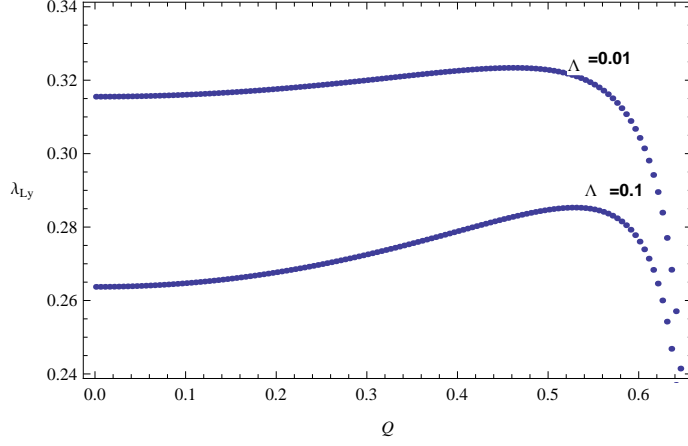


Figure 23: The figure shows λ_{Ly} vs Q for massless particles for the BIdS black hole for different values of Λ . Here $M = 0.6, b = 1$

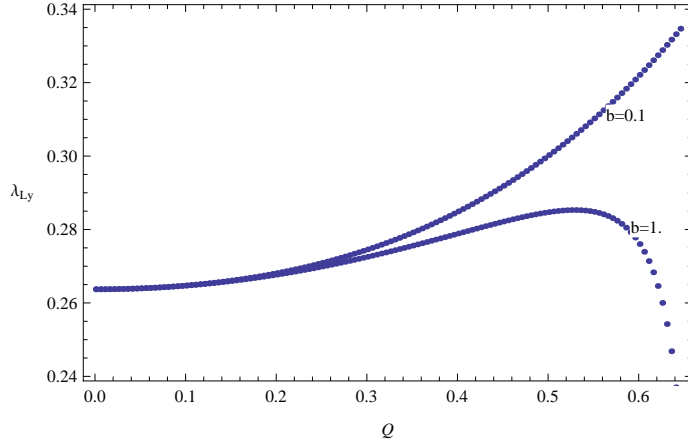


Figure 24: The figure shows λ_{Ly} vs Q massless particles for the BIdS black hole for two values of the BI parameter $b = 0.1, 1$. Here $M = 0.6, \Lambda = 0.1$

For the light trajectories calculated from the effective metric, the Lyapunov exponent is

$$\lambda_{Ly}^2 = \frac{fr^2}{2} \left[\frac{f}{r^2} \frac{G_m}{G_e} \left(\frac{G_e}{G_m} \right)'' - \left(\frac{f}{r^2} \right)'' \right] \quad (35)$$

here, λ_{Ly} for the BIdS black hole is given by

$$\lambda_{Ly}^2 = \frac{f}{r^3(Q^2/b^2 + r^4)} \left[-\frac{10}{3} \frac{Q^2}{b^2} \Lambda r^3 + \left(8 \frac{Q^2}{b^2} - 12r^4 \right) \left(\frac{Q^2}{3} \sqrt{\frac{b}{Q}} F(r) - M \right) \right]$$

$$+ \frac{Q^2 r}{3} [20r^2 - 26\sqrt{Q^2/b^2 + r^4}] + 7\frac{Q^2}{b^2}r - 3r^5], \quad (36)$$

with $F(r)$ denoting the elliptic function eq.(6).

In Fig.(23) the Lyapunov exponent versus Q is shown for two different values of Λ for massless particles. As the charge grows the difference diminishes. In Fig.(24) the Lyapunov exponent versus Q for massless particles is shown for two different values of b . As the BI parameter b grows the BIidS approaches the RNdS behavior. So far we found agreement between the QNM at the high-frequency limit and the ones obtained using the WKB method, that tells us that the frequency of the perturbation does not influence the black hole response. In summary, the black hole is stable for large Q and small Λ .

In Figs.(25) and Fig(26) the real part of the QNM are displayed. They are proportional to Ω_a . The plots correspond to the following equations, for the massless test particles,

$$\Omega_a^2 = \frac{f(r)}{r^2} \quad (37)$$

evaluated at the roots of eq. (26); while for photons

$$\Omega_a^2 = \frac{G_m f(r)}{G_e r^2} \quad (38)$$

evaluated at the roots of eq.(32). In Fig.(25), Ω_a of BIidS is plotted vs. Q for two values of the BI parameter, $b = 0.05$ and $b = 0.1$ and compared with RNdS. As b grows Ω_a approaches the behavior of RNdS. Nonlinear electromagnetism is to suppresses Ω_a . In Fig.(26) Ω_a versus Q is shown for massless particles. Comparison is done for two different values of Λ . As Λ grows the value of Ω_a decreases.

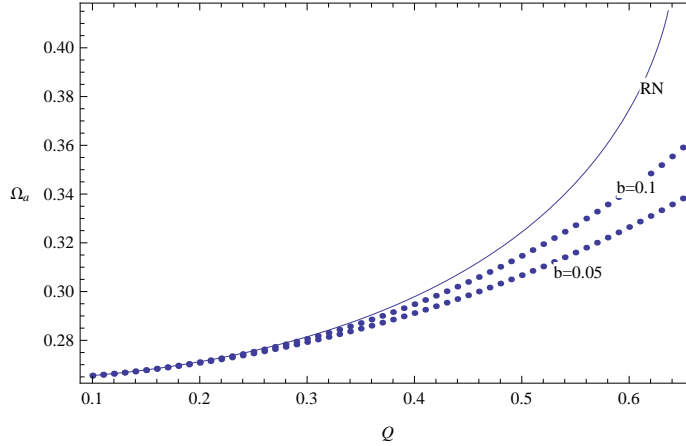


Figure 25: The figure shows Ω_a vs Q for the massless test particles. Here $M = 0.6, \Lambda = 0.1$

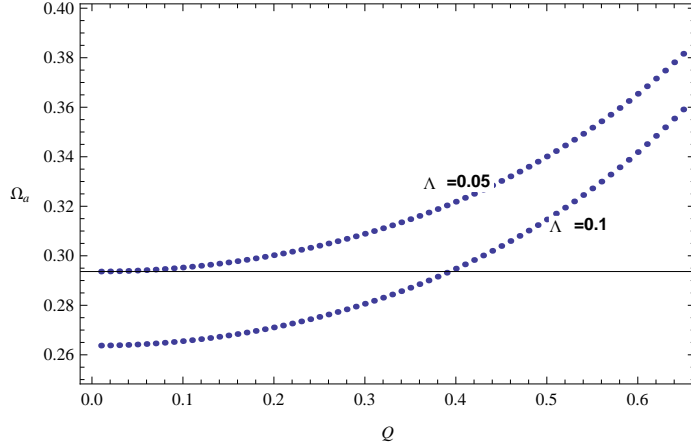


Figure 26: The figure shows Ω_a vs Q for massless particles. Here $M = 0.6, b = 0.1$.

In Fig.(27) the Lyapunov exponent corresponding to massless test particles and photons is compared. In Fig.(28) Ω_a for massless test particles is compared with the one of light rays or photons.

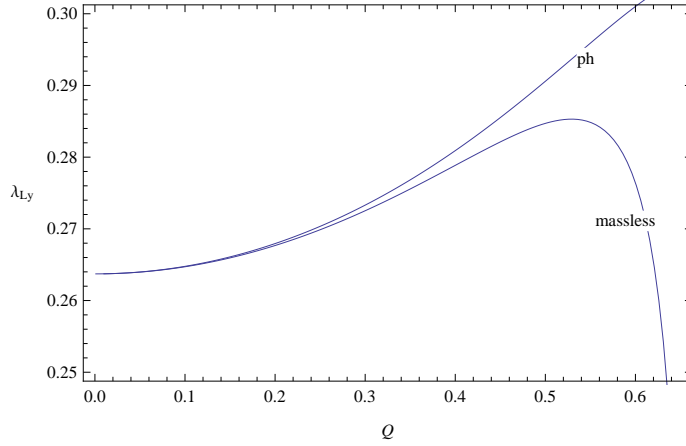


Figure 27: The figure shows λ_{Ly} vs Q for photons and massless test particles. $M = 0.6, \Lambda = 0.1, b = 1$

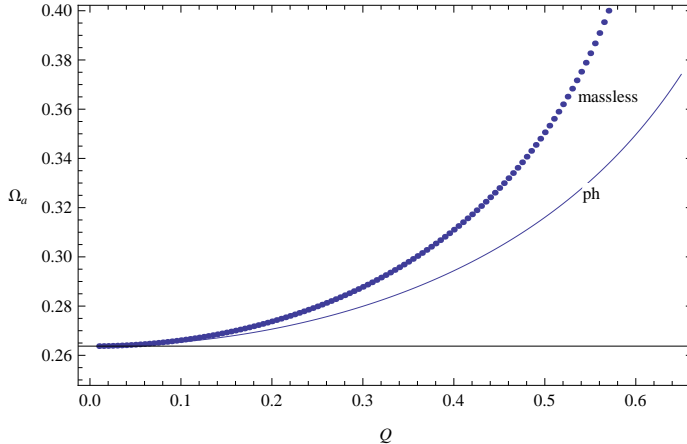


Figure 28: The figure shows Ω_a vs Q for photons and massless particles. $M = 0.6$, $\Lambda = 0.1$, $b = 1$

6 Absorption cross sections at low and high energy frequency limits

Another important aspect to study when a black hole is perturbed by a test field is how much of the impinging field is absorbed by the black hole. Accretion rates and the growth of the mass of a black hole are related to the magnitude of the absorption cross section. In this section, we will calculate the absorption cross section, in the low and high-frequency limits, for both the scalar and electromagnetic field via null geodesics.

The low-frequency absorption cross section for minimally-coupled scalar massless field of a static black hole has been computed to be equal to the horizon area of the black hole by Das et.al. [60]

In Fig(29) the area of the event horizon, $A = \pi r_h^2$ has been plotted for both the RNdS and the BIdS black holes for comparison, with $M = 1$, $\Lambda = 0.01$ and $b = 0.2$. The BIdS area turned out to be bigger than the one for RNdS. Hence, the absorption cross section is larger for the BIdS black hole. In this case a distinction is not made between photons and massless test particles, since the horizon is the same for both particles.

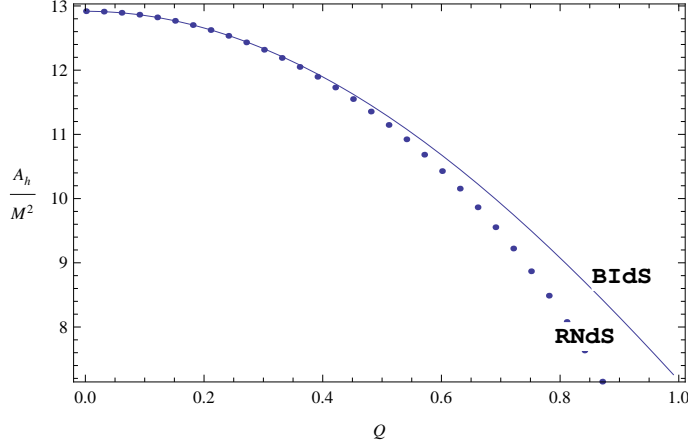


Figure 29: The figure shows the area of the event horizon A_h/M^2 vs Q . $M = 1$, $\Lambda = 0.01$ and $b = 0.2$

In the high-frequency limit the absorption cross section can be considered as the classical capture cross section generated by the null geodesics in the case of massless scalar waves. In this limit the absorption cross section is also called geometric cross section, σ_{geo} , and it is given by

$$\sigma_{\text{geo}(\text{scalar})} = \pi\beta_{\text{null}}^2 = \frac{\pi r_{\text{null}}^2}{f(r_{\text{null}})}, \quad (39)$$

Here, r_{null} is the radius of the unstable circular orbit obtained from $\frac{dV_{\text{null}}}{dr} = 0$, and β is the impact parameter given by $\beta = \frac{L}{E}$ where L is the angular momentum and E is the energy of the test particle at infinity. β_{null} corresponds to the value for the unstable circular orbit. V_{null} and β_{null} are related by,

$$V_{\text{null}} = \frac{E_{\text{null}}^2}{L_{\text{null}}^2} = \frac{1}{\beta_{\text{null}}^2}. \quad (40)$$

For photons, to calculate σ_{geo} , one has to consider the effective metric as was done in section(5). Hence the corresponding geometric cross section for the photon is given by,

$$\sigma_{\text{geo}(\text{photons})} = \frac{\pi r_{\text{null}}^2}{f(r_{\text{null}})G_e(r_{\text{null}})}, \quad (41)$$

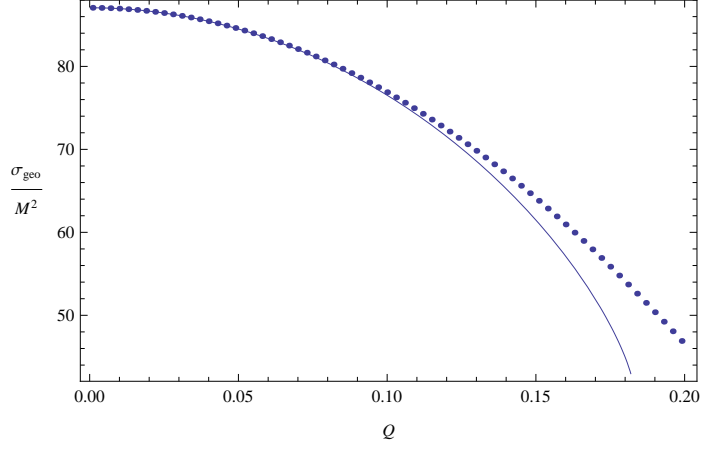


Figure 30: The figure shows $\frac{\sigma_{geo}}{M^2}$ vs Q for the massless scalar for BIdS and RNdS black holes. The continuous curve is for RNdS and the dotted one is for BIdS black hole. Here $M = 0.01715$, $\Lambda = 0.0973$, $b = 0.5$

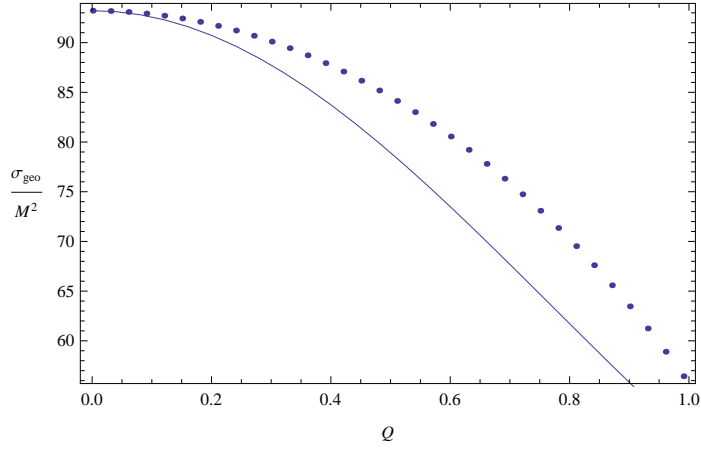


Figure 31: The figure shows σ_{geo}/M^2 vs Q for the massless scalar field and the photons for the BIdS black hole. The continuous curve is for the photons and dotted is for the scalar field. Here $M = 1$, $\Lambda = 0.01$, and $b = 0.2$

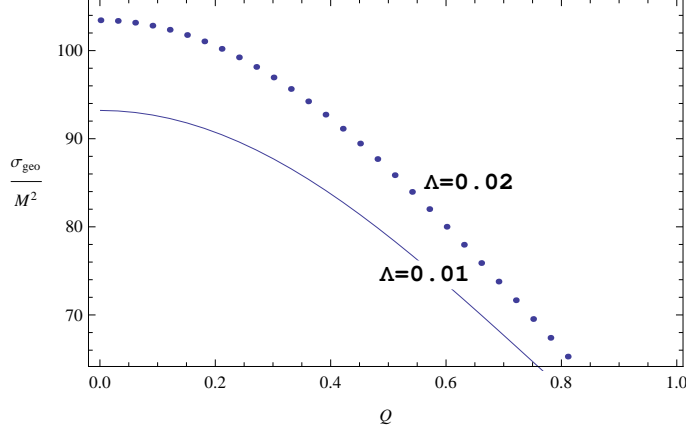


Figure 32: The figure shows σ_{geo}/M^2 vs Q for photons for two values of Λ . Here $M = 1, b = 0.2$

In Fig(30) the geometric cross section for massless test particles of RNdS and BIdS is illustrated as a function of the electric charge Q . The continuous curve is for the RNdS black hole while the dotted is for BIdS; σ_{geo} is smaller for RNdS than the one of BIdS. In Fig(31) the geometric cross section for BIdS comparing the one for massless test particles with the one corresponding to photons is illustrated as a function of the electric charge Q . The continuous curve corresponds to photons while the dotted one is for massless test particles. The absorption is higher for massless particles. In Fig(32) the geometric cross section from BIdS black hole for photons is illustrated as a function of the electric charge Q and the comparison is done between two different values of Λ , $\Lambda = 0.01$ and $\Lambda = 0.02$, as the labels on each curve show. The geometric cross section increases with Λ .

Decanini et.al [61] showed that the oscillatory part of the absorption cross section in the eikonal limit can be written in terms of the parameters of the unstable null circular orbits, the Lyapunov exponent λ_{LY} and the angular velocity Ω_a as follows:

$$\sigma_{osc} = -\frac{4\pi\lambda_{LY}}{\omega\Omega_a^2} e^{-\frac{\pi\lambda_{LY}}{\Omega_a}} \sin\left(\frac{2\pi\omega}{\Omega_a}\right), \quad (42)$$

where ω is the oscillating frequency of the scalar field. Therefore the high-frequency limit of the absorption cross section is proportional to the sum of σ_{osc} and σ_{geo} ,

$$\sigma_{abs}^{hf} = \frac{\pi r_{null}^2}{f(r_{null})} \left(1 - \frac{4\lambda_{LY}}{\omega} e^{-\frac{\pi\lambda_{LY}}{\Omega_a}} \sin\left(\frac{2\pi\omega}{\Omega_a}\right)\right), \quad (43)$$

The above is known as the sinc approximation in the literature. Macedo and Crispino studied absorption cross sections for a massless scalar wave in Bardeen black hole [62]. They calculated absorption cross section via the sinc approximation as well as numerically solving the equations for each ω . For Bardeen black hole they showed

that the sinc approximation agree remarkably well not only at high frequency limit, but also at the intermediate frequencies.

In the Fig(33) the absorption cross section in the sinc approximation is presented for massless test particles for RNdS and BIdS, as a function of the frequency ωM . The BIdS absorption cross section is greater than the RNdS. In the Fig(34) the absorption cross section in the sinc approximation from massless test particles impinging on the BIdS black holes, as a function of the frequency ωM , is illustrated for two values of Λ , $\Lambda = 0.01$ and $\Lambda = 0.02$. As Λ increases σ_{abs} also increases. In the Fig(35) the absorption cross section for BIdS as a function of ωM is illustrated, comparing the one for massless test particles and the photons. It can be seen that σ_{abs} for photons is suppressed as compared to massless particles, i.e. the latter are more easily captured by the BIdS black hole (Figs. 31 and 35).

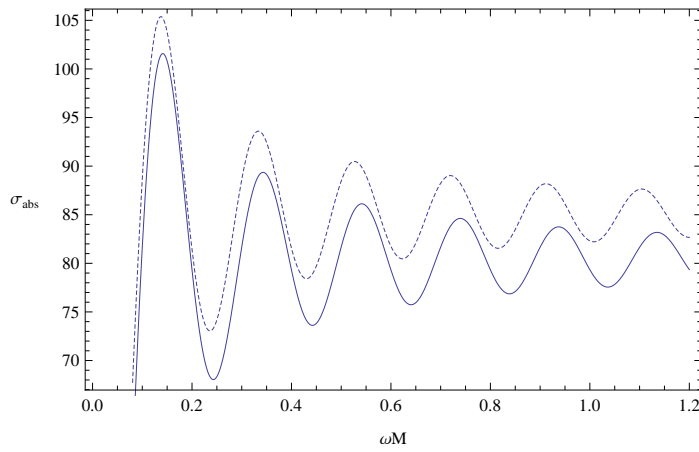


Figure 33: The figure shows σ_{abs} vs ωM for the massless scalar field for RNdS and BIdS. The continuous curve is for the RNdS black hole while the dotted one is for BIdS. Here, $M = 1, \Lambda = 0.01, Q = 0.6$ and $b = 0.01$

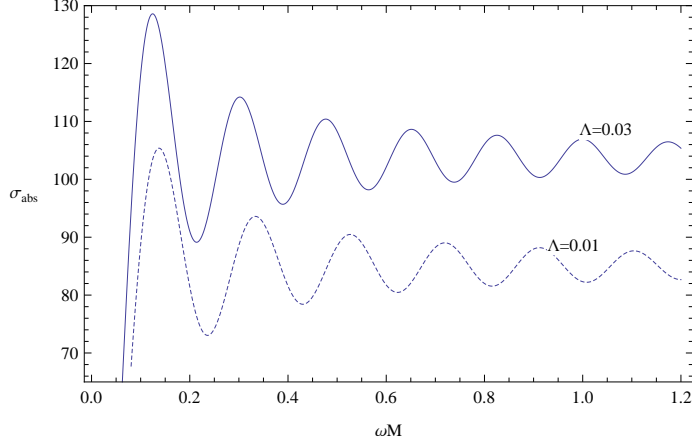


Figure 34: The figure shows σ_{abs} vs ωM for the massless scalar field for the BIdS. Here, $M = 1, b = 0.01, Q = 0.6$.

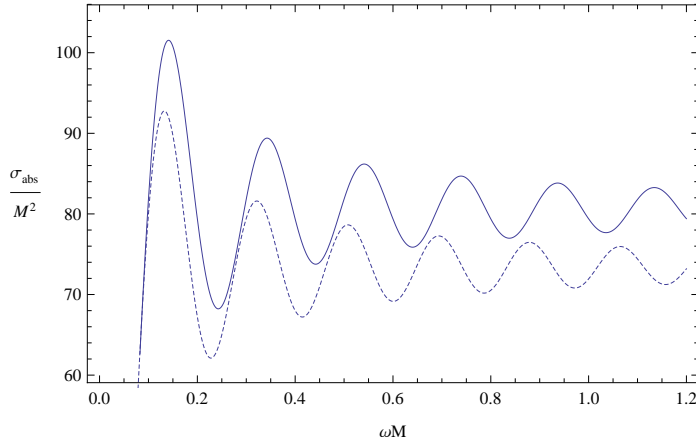


Figure 35: The figure shows σ_{abs} vs ωM for the BIdS. Here. the massless test particles is given in continuous curve with the corresponding one for photons given by the dotted curve. Here, $M = 1, \Lambda = 0.01, Q = 0.6, b = 0.2$

7 Conclusions

In this paper, we have studied Born-Infeld black hole with a positive cosmological constant (BIdS). These black holes have interesting characteristics so that both time-like and space-like singularities exists depending on the parameters chosen. The main purpose of this paper has been to study the QNM's for the massless and photons. We also have presented absorption cross sections.

First massless scalar fields perturbation is analyzed with the WKB approximation. QNM frequencies were calculated for all parameters, M, Q, Λ, l and b . When Q is increased, ω_r, ω_i and the quality factor increases; BIdS black hole is stable for large charge and it is a better oscillator for large charge. When Λ increases, ω_r, ω_i and the quality factor decreases; the black hole is more stable for smaller Λ . When the non-linear parameter b is increased, ω_r increases to reach a stable value; ω_i increases to a maximum and decreases for large b . Hence there is value of b that the black hole reach it's maximum stability. The quality factor also increases with b . Hence RNdS black hole is a better oscillator compared to the BIdS black hole.

When ω is analyzed with respect to l , we observed that ω_r increases linearly with respect to l ; ω_i decreases and reach a stable value for larger l . Hence the black hole is more stable for smaller values of l . We also computed ω with respect to n , the number of harmonics. When n increases, ω_r decreases and ω_i increases; the fundamental frequency takes the longest time to decay and the oscillating frequency is higher for smaller harmonics.

All the *WKB* calculations were done for $l > 0$ values. We observed that for $l = 0$, the potential has a negative region and a local minima in between the horizons; one cannot apply WKB method to compute QNM frequencies of $l = 0$ case. It would be interesting to apply another method to study the QNM frequencies and see if the BIdS black hole is stable for $l = 0$ case.

In the second half of the paper null geodesic of the black hole were employed to study the QNM frequencies and the absorption cross sections at the eikonal limit. The real part of ω is proportional to the angular velocity of the null geodesics, Ω_a . The imaginary part of ω is proportional to the Lyapunov coefficient, λ_{Ly} .

First, QNM frequencies for both massless and photons were calculated via the angular velocity and the Lyapunov coefficient of the null geodesics. In black holes with non-linear electrodynamics, the photons follow null geodesics of an effective geometry. The massless particles follow the usual null geodesics of the black hole geometry.

When Q is increased QNM's for the BIdS increases and QNM's for the RNdS increases to a maximum and then decreases. When observed ω_i with respect to Q , higher value of Λ has lower ω_i similar to what was obtained with the WKB analysis. For massless particles, ω_r increases with Q and the value is higher for larger b (for the same Q). RNdS black hole has a larger ω_r than the BIdS black hole. When plotted for BIdS black hole alone, ω_r is smaller for larger value of Λ .

When λ_{Ly} is plotted, the photons have a higher value than the massless particles. Hence the black hole is more stable for electromagnetic perturbations. On the other hand ω_r is larger for the massless particles when compared with the photons.

The absorption cross sections were studied for both BIdS and RNdS black holes. At low frequencies, the absorption cross section for massless particles is higher for the BIdS; BIdS black hole is a better absorber of the massless scalar waves.

At higher frequencies, the absorption cross section is given by the geometric cross

section. Here BI_dS black hole has a larger σ_{geo} compared to RN_dS for massless particles. For the BI_dS black hole, σ_{geo} is larger for the massless scalar field than for the photons. Computations are done for the BI_dS by varying Λ . When Λ is larger, σ_{geo} is larger.

The high frequency limit of the absorption cross section was also calculated by the sink approximation given by σ_{abs} . When σ_{abs} vs ωM is plotted for the massless particles, σ_{abs} is higher for the BI_dS black hole. Also, σ_{abs} is larger for higher Λ for the BI_dS black hole. Hence the BI_dS absorbed more for larger cosmological constant. When σ_{abs} is compared for the photons and the massless particles, the massless particles has higher absorption.

Acknowledgments: SF wish to thank R. A. Konoplya for providing the *Mathematica* file for the WKB approximation.

References

- [1] M. Born and L. Infeld, *Foundations of the new field theory*, Proc. Roy. Soc. Lond. **A144** (1934) 425.
- [2] G. W. Gibbons and D. A. Rasheed, *Electromagnetic duality rotations in nonlinear electrodynamics*, hep-th/9506035
- [3] G. Boillat, *Nonlinear electrodynamics: Lagrangians and equations of motion*, Jour. Math. Phys. **11** 3, 941 (1970)
- [4] Y. N. Obukhov, and G. F. Rubilar, *Fresnel analysis of the wave propagation in nonlinear electrodynamics*, Phys. Rev. **D 66** 024042 (2002)
- [5] R. G. Leigh, *Dirac-Born-Infeld action from Dirchlet σ -model*, Mod. Phys. Lett **A4** (1989) 2767.
- [6] A. A. Tseytlin, *Vector field effective action in the open superstring theory*, Nucl. Phys. **B 276** 393 (1986)
- [7] R. R. Metsaev, M. A. Rahmanov, and A. A. Tseytlin, *The Born-Infeld action as the effective action in the open superstring theory*, Phys. Lett. **B 193** 2017 (1987)
- [8] E. Bergshoeff, E. Sezgin, C. N. Pope, and P. K. Townsend, *The Born-Infeld action from conformal invariance of the open superstring theory*, Phys. Lett. **B 188** 70 (1987)
- [9] G. W. Gibbons, *Aspects of Born-Infeld Theory and String/M-Theory*, Rev.Mex.Fis.49S1:19-29 (2003), hep-th/0106059

- [10] N. Bretón, *Geodesics structure of the Born-Infeld black holes*, Class. Quan. Grav. **19** 601 (2002)
- [11] R. Linares, M. Maceda, and D. Martínez, *Test particle motion in the Born-Infeld black hole*, Phys. Rev. **D 92** 024052 (2015)
- [12] S. Fernando, *Remarks on null geodesics of Einstein-Born-Infeld black holes*, ISRN Math. Phys. 869069 (2012)
- [13] S. Fernando, *Gravitational perturbation and quasi-normal modes of charged black holes in Einstein-Born-Infeld gravity*, Gen. Rel. Grav. **37** 585 (2005)
- [14] S. Fernando and C. Holbrook, *Stability and quasi normal modes of charged black holes in Born-Infeld gravity*, Int. Jour. Theo. Phys. **45** 1630 (2006)
- [15] S. Fernando, *Decay of massless Dirac field around the Born-Infeld black hole*, Int. Jour. Mod. Phys. **A 25** (2010) 669
- [16] S. Fernando, *Born-Infeld-de Sitter gravity: cold, ultra cold and Nariai black holes*, Int. Jour. Mod. Phys. **D 22** 1350080 (2013)
- [17] J. P. Pereira, and J. A. Rueda, *Energy decomposition within Einstein-Born-Infeld black holes*, Phys. Rev. **D 91** 064048 (2016)
- [18] N. Bretón, *Energy extraction from the Einstein-Born-Infeld black holes*, arXiv:1611.08584
- [19] G. W. Gibbons and C. A. R. Herdeiro, *The Melvin Universe in Born-Infeld theory and other theories of non-linear electrodynamics*, Class. Quant. Grav. **18** 1677 (2001)
- [20] M. Aiello, R. Ferro and G. Girbet, *Exact solutions of Lovelock-Born-Infeld black holes*, Phys. Rev. **D 70** 104014 (2004)
- [21] X. Gao, *Non-supersymmetric attractors in Born-Infeld black holes with a cosmological constant* JHEP, 0711:006 (2007)
- [22] M. Cataldo and A. Garcia, *Three dimensional black hole coupled to the Born-Infeld electrodynamics*, Phys. Lett. **B 456**, 28 (1999)
- [23] S. Fernando and D. Krug, *Charged black hole solutions in Einstein-Born-Infeld gravity with a cosmological constant*, Gen. Rel. Grav. **35**, 129 (2003)
- [24] T. K. Dey, *Born-Infeld black holes in the presence of a cosmological constant*, Phys.Lett. B **595**, 484 (2004).
- [25] R. Cai, D. Pang and A. Wang, *Born-Infeld black holes in (A)dS spaces*, Phys. Rev. **D 70**, 124034 (2004)

- [26] B. P. Abbott et al. (LIGO Scientific and Virgo Collaborations), *Binary Black Hole Mergers in the First Advanced LIGO Observing Run*, Phys. Rev. **X** **6** 041015 (2016)
- [27] S. R. Dolan, L. A. Oliveira, and L. C. B. Crispino, *Quasinormal modes and Regge Poles of the canonical acoustic hole*, Phys. Rev. **D** **82** 084037 (2010)
- [28] J. Li, K. Lin, and N. Yang, *Nonlinear electromagnetic quasi normal modes and Hawking radiation of a regular black hole with magnetic charge*, Eur. Phys. Jour. **C** **75** 75 (2015)
- [29] C. Chirenti and M. G. Rodrigues, *A comparison between different cosmological models using black hole quasi normal modes*, Phys. Rev. **D** **92** 084051 (2015)
- [30] K. Lin and W. Qian, *A matrix method for quasi normal modes: Schwarzschild black holes in asymptotically flat and (anti)-de Sitter space-times*, arXiv:1610.08135
- [31] M. Richartz, *Quasinormal modes of extremal black holes*, Phys. Rev. **D** **93** 064062 (2016)
- [32] H. T. Cho, A. S. Crnell, J. Doukas, T. R. Huang, and W. Naylor, *A new approach to black hole quasi normal modes: a review of the Asymptotic Iteration Method*, Adv. Math. Phys. 281705 (2012)
- [33] R. A. Konoplya and A. Zhidenko, *Instability of higher dimensional charged black holes in the de-Sitter world*, Phys. Rev. Lett. **103**, 161101 (2009)
- [34] R. A. Konoplya and A. Zhidenko, *Instability of D-dimensional extremally charged Reissner-Nordstrom(-de Sitter) black holes: Extrapolation to arbitrary D*, Phys. Rev. D **89**, no. 2, 024011 (2014)
- [35] R. A. Konoplya and A. Zhidenko, *Decay of a charged scalar and Dirac fields in the Kerr-Newman-de Sitter background*, Phys. Rev. D **76**, no. 8, 084018 (2007) Erratum: [Phys. Rev. D **90**, no. 2, 029901 (2014)]
- [36] R. A. Konoplya and A. Zhidenko, *High overtones of Schwarzschild-de Sitter quasinormal spectrum*, JHEP **0406**, 037 (2004)
- [37] E. Berti, V. Cardoso, and A. O. Starinets, *Quasinormal modes of black holes and black branes*, Class. Quan. Grav. **26** 163001 (2009)
- [38] S. Perlmutter et al., *Measurements of Ω and Λ from 42 high-redshift supernovae*, Astrophys. J. **517** 565 (1999)

- [39] A.G. Riess et. al., *Observational evidence from supernovae for an accelerating universe and a cosmological constant*, Astron. J. **116** 1009 (1998); *BVRI Light Curves for 22 Type Ia Supernovae*, Astron. J. **117** 707(1999)
- [40] D. N. Spergel et.al. (WMAP Collaboration), *Wilkinson Microwave Anisotropy Probe (WMAP) three year results: implications for cosmology*, Astrophys. J. Suppl. **170** 377 (2007)
- [41] M. Tegmark et.al. (SDSS Collaboration) *Cosmological parameters from SDSS and WMAP* , Phys. Rev. **D 69** 103501 (2004)
- [42] U. Seljak et.al., *Cosmological parameter analysis including SDSS Ly α forest and galaxy bias: constraints on the primordial spectrum of fluctuations, neutrino mass, and dark energy*, Phys. Rev. **D 71** 103515 (2005)
- [43] S. Fernando, *Spinning dilaton black holes in 2+1 dimensions: quasinormal modes and the area spectrum*, Phys. Rev. **D 79** 124026 (2009)
- [44] S. Fernando, *Quasinormal modes of charged scalars around dilaton black Holes in 2+1 dimensions: exact frequencies*, Phys. Rev. **D 77** 124005 (2008)
- [45] S. Fernando, *Quasinormal modes of charged dilaton black holes in 2+1 dimensions*, Gen. Rel. Grav. **36** 71 (2004)
- [46] S. Iyer and C.M. Will, *Black-hole normal modes: A WKB approach. I. Foundations and application of a higher-order WKB analysis of potential-barrier scattering*, Phys. Rev. **D 35** 3621(1987)
- [47] R. A. Konoplya, *Quasinormal behavior of the D-dimensional Schwarzschild black hole and higher order WKB approach*, Phys. Rev. **D 68** 024018 (2003)
- [48] S. Fernando, *Regular black holes in de Sitter universe: scalar field perturbations and quasinormal modes*, Int. Jour. Mod. Phys. **D 24** 1550104 (2015)
- [49] S. Fernando and T. Clark, *Black holes in massive gravity: quasinormal modes of scalar perturbations*, Gen. Rel. Grav. **46** 1834 (2014)
- [50] R. Konoplya, *Quasinormal modes of the charged black hole in Gauss-Bonnet gravity*, Phys. Rev. **D 71** 024038 (2005)
- [51] V. P. Frolov, and I. D. Novikov, *Black hole physics: basic concepts and new developments*, Kluwer Academic Publishers, (1998)
- [52] V. Cardoso, A.S. Miranda, E. Berti, H. Witek and V.T. Zanchin, *Geodesic stability, Lyapunov exponents and quasinormal modes*, Phys.Rev. **D 79** (2009) 064016

- [53] B. Mashhoon, *Stability of charged rotating black holes in the eikonal approximation*, Phys. Rev. **D 31** 290 (1985)
- [54] S. R. Dolan, *The quasinormal mode spectrum of a Kerr black hole in the eikonal limit*, Phys. Rev. **D 82** 104003 (2010)
- [55] S. Hod, *Black-hole quasinormal resonances: wave analysis versus a geometrical-optics approximation*, Phys. Rev. **D 80** 064004 (2009)
- [56] J. Morgan, V. Cardoso, A. S. Miranda, C. Molina and V. T. Zanchin, *Quasinormal modes of black holes in anti-de Sitter space: a numerical study of the eikonal limit*, Phys. Rev. **D 80** 024024 (2009)
- [57] N. Bretón, and L. A. Lopez, *Quasinormal modes of nonlinear electromagnetic black holes from unstable nullgeodesics*, Phys. Rev. **D 94** 104008 (2016)
- [58] M. Novello, V. A. De Lorenci, J. M. Salim, and R. Klippert, *Geometrical aspects of light propagation in nonlinear electrodynamics*, Phys. Rev. **D 61** 045001 (2000)
- [59] S. A. Gutierrez, A. L. Dudley, and J. F. Plebanski, *Signals and discontinuities in general relativistic nonlinear electrodynamics*, Jour. Math. Phys. **22** 2835 (1981)
- [60] S. R. Das, G. Gibbons, and S. D. Mathur, *Universality of low energy absorption cross sections for black holes*, Phys. Rev. Lett. **78** 417 (1997)
- [61] Y. Decanini, G. Esposito-Farese and A. Folacci, *Universality of high-energy absorption cross sections for black holes* Phys. Rev. **D 83** 044032 (2011)
- [62] Caio F. B. Macedo and Luis C. B. Crispino, *Absorption of planar massless scalar waves by Bardeen black holes* Phys. Rev. **D 90** 064001 (2014)